ARCHIVES OF ELECTRICAL ENGINEERING VOL. 74(1), pp. 85–103 (2025)

DOI 10.24425/aee.2025.153014

Design and optimization of an improved hybrid permanent magnets Vernier machine with less-rare-earth and high torque density

HUI LI ✉

School of Intelligent Manufacturing and Materials Engineering
Gannan University of Science and Technology
156 Hakjia Avenue, Ganzhou, Jiangxi Province, China
e-mail: ✉ *Lihui_gnust@163.com*

(Received: 26.07.2024, revised: 31.01.2025)

Abstract: This paper proposes a novel improved hybrid permanent magnet Vernier machine (IHPMVM), which is characterized by less-rare-earth (LRE) and high torque-density. The proposed machine features a hybrid magnet arrangement, which adopts both rare earth (RE) and LRE magnets in one magnetic pole simultaneously. The proposed improved design can reduce the consumptions of RE materials by employing low-cost LRE magnets in place of RE magnets. Besides, the hybrid magnet arrangement design has a good magnetic flux-concentrated effect, resulting in high torque density. Particularly, dummy slots are introduced to achieve a flux modulation effect. This unique design effectively reduces the inevitable leakage flux, thereby further improving the utilization of PMs and torque density. Firstly, the machine configuration and its improved design are introduced and investigated. Then, a multi-objective optimization is carried out to obtain the optimal design of the proposed machine considering comprehensive performance. Furthermore, the preliminary electromagnetic characteristics of the proposed machine are compared and analyzed using finite element (FE) methods, which verifies the effectiveness of the optimization. Finally, the demagnetization risk of the LRE magnets is evaluated. This paper is expected to provide a technical reference for designing LRE machines.

Key words: flux modulation effect, hybrid magnets, less-rare-earth, multi-objective optimization, Vernier machine

1. Introduction

Permanent magnet machines (PMMs) are widely used in wind power generation and industrial applications due to their advantages of high torque density, and high efficiency [1–3]. However, conventional PMMs are usually paired with mechanical transmission devices, resulting in reduced efficiency and redundant structure. Thus, direct drive PMMs have been developed gradually thanks to their excellent accuracy and high efficiency, eliminating the mechanical transmission devices [4,5].

Recently, permanent magnet Vernier machines (PMVMs) have attracted widespread research and attention due to their simple structure and high torque density at low speeds, which are considered promising candidates for direct drive systems. [6–8]. The PMVM can achieve high toque density through the flux modulation effect, and numerous harmonics in the air gap magnetic field are serving as working harmonics [6]. Over the past decade, various PMVMs have been investigated and studied [6–14], including structures [9–12], theories [6, 7, 13] and control strategies [14], with current research primarily concentrating on topology design and improvement of power factor. For example, a dual-stator PMVM design is proposed in [11], which enhances the air gap magnetic flux density, thereby improving the torque capability. Besides, a hybrid excited PMVM is proposed in [12], in which a mixed excitation structure uses auxiliary DC excitation on the stator side.

On the other hand, various PMVMs with different magnet arrangements have been extensively studied, such as dual PM [15, 16], interior PM [17, 18], and consequent-pole PM configurations [19, 20]. To enhance the air-gap flux density harmonics, certain dual-PM Vernier machines, presented in [15, 16], demonstrate a bi-directional flux modulation effect, contributing to rich harmonics for torque generation. Additionally, interior PM Vernier structures, such as V-shaped PM [17] and spoke-type PM configurations [18], have been developed to enhance the concentrated flux effect, resulting in higher torque capability compared to the surface-mounted PMM. Nonetheless, the spoke-type PMs act as barriers to air flux for low-order working harmonics, creating a flux barrier effect that compromises electromagnetic performance [18]. To address these issues, proposals include non-uniformly distributed auxiliary teeth [19] and alternating flux barrier designs [17], offering a magnetic path for low-order harmonics and thereby enhancing torque capability compared to conventional approaches. Moreover, the consequent-pole PM Vernier machine, due to its asymmetrical air-gap field distribution [19] and doubly salient structure [20], exhibits significant improvements in low-order working harmonics. Generally, to obtain high torque density, conventional PMVMs usually adopt magnets with high coercivity force. However, high coercivity magnets typically incorporate rare earth (RE) materials [21], which are costly and subject to supply instability.

Therefore, to alleviate the RE magnets consumptions, less-rare-earth (LRE) magnets with lower energy product are considered as alternatives in PM machines [21–27]. Particularly, spoke-type ferrite PM machines with flux-concentrating effect are competitive in LRE machines [23–25]. This is attributed to their unique magnet arrangements, which can generate high air gap flux density and suffer a relatively low demagnetization risk. However, spoke-type ferrite PM machines use considerable magnets, which limits design flexibility. Moreover, novel structures utilizing different PM types have been investigated [26, 27], reducing the cost of RE materials. However, employments of less-rare-earth magnets usually result in a compromised torque density and unexpected irreversible demagnetization, thereby degrading overall performance.

Therefore, to address the issues, a novel improved hybrid permanent magnet Vernier machine (IHPMVM) is proposed in this paper. The proposed IHPMVM utilizes a hybrid magnet arrangement that incorporates different types of magnets simultaneously. This design offers strong anti-demagnetization capability by strategically placing RE magnets to counter demagnetization. Thus, the consumption of RE materials can be reduced by using low-cost LRE magnets in the magnetic poles, realized by replacing the RE magnets. Besides, the proposed machine can also achieve the excellent torque capability due to the flux-concentrated of hybrid magnet arrangement and flux modulation effect. Finally, the proposed machine exhibits characteristics of LRE and high torque-density.

This paper is structured as follows. In Section 2, the improved design and operating principle of the proposed machine is introduced, and the torque production mechanism is also studied. Then, a multi-objective optimization progress is carried out to obtain the optimal design in Section 3. In Section 4, the preliminary electromagnetic performances are analyzed and simulated in details using finite element (FE) methods, including open-circuit characteristic *et al*. Finally, conclusions are drawn in Section 5.

2. Improved design and operating principle

2.1. Improved design and machine configuration

Firstly, an improved hybrid magnet design is proposed in this paper, depicted by its topology evolution in Fig. 1(a). In the conventional PMVM, V-shaped RE magnets and dummy slots are adopted and designed in the rotor iron. Correspondingly, LRE magnets are introduced to replace the RE magnets in the second-layer magnets. In the proposed design, a single-layer RE magnets are set with the LRE magnets, forming a delta-type magnet arrangement. Such a design can achieve a good torque capability due to the flux-concentrated effect. Besides, the first-layer RE magnets can also prevent the second-layer LRE magnets from irreversible demagnetization caused by armature reaction.

The proposed machine adopts 24 slots and 19 pole pairs, which can utilize the flux modulation effect to generate output torque, as shown in Fig. 1(b). The stator adopts an open-slot structure, with each stator tooth and dummy slots serving as modulation blocks. This achieves flux modulation in the proposed machine, with numerous harmonics in the air gap magnetic field serving as effective components. The PM flux will flow into the stator side between the two dummy slots, and the dimensions of the dummy slots can be adjusted to reduce cogging torque and torque ripple. The winding configuration diagram of the proposed machine is shown in Fig. 2.

2.2. Operating principle

The proposed IHPMVM features 24 slots and 19 pole pairs, consequently, a series of harmonics will be generated by the permanent magnets in the air gap after being modulated by the dummy slots and stator teeth. The number of air gap harmonics can be expressed as:

$$P_{n,m} = |np_r \pm mN_s| (n = 1, 3, 5, \ldots, \infty; m = 0, 1, 2 \ldots \infty), \tag{1}$$

in which N_s and p_r are the tooth number of the stator and rotor. Thus, the rotation speed of each air gap harmonic $\omega_{n,m}$ can be expressed as:

$$\omega_{n,m} = \frac{\pm np_r}{np_r \pm mN_s}\omega_r, \tag{2}$$

where ω_r is the angular speed of the rotor, and the air gap magnetic flux generated by the armature reaction will produce a series of harmonic components in the air gap through modulation between the rotor and stator teeth. The number of air gap harmonics can be represented as:

$$P_{u,v} = |vp_r \pm u| (v = 1, 2, 3, \ldots, \infty; \quad u = 0, 1, 2, 4, 5, 7 \ldots \infty). \tag{3}$$

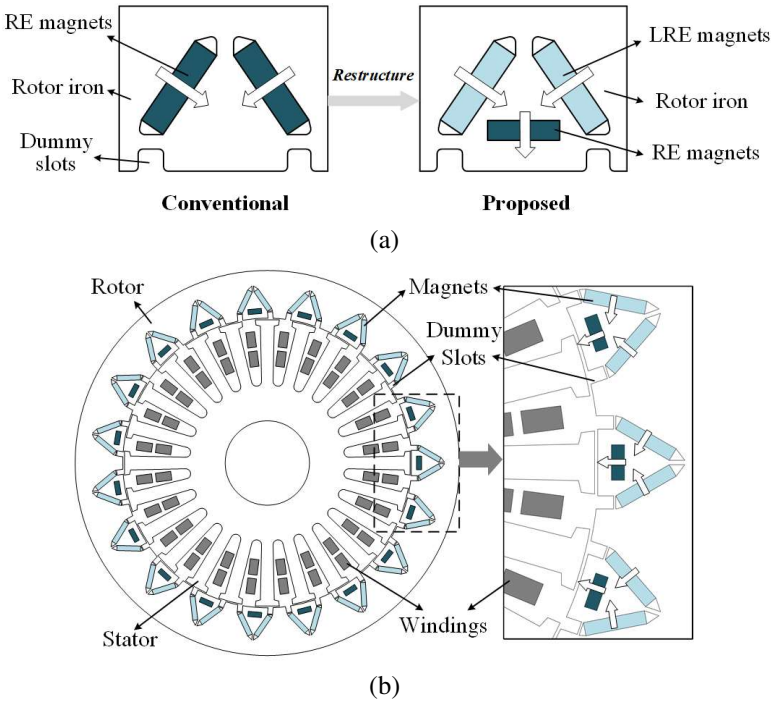

Fig. 1. Improved design of the proposed IHPMVM: (a) topology evolution; (b) machine configuration

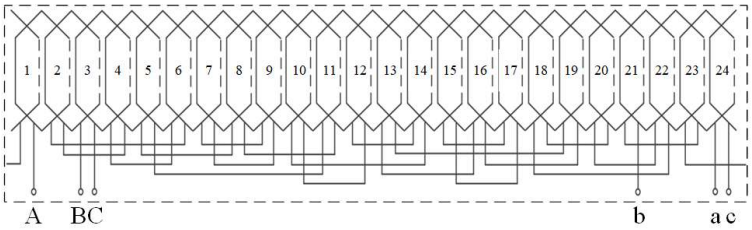

Fig. 2. Windings configuration

The corresponding rotational speed of each air gap harmonic generated by the armature reaction modulation can be expressed as:

$$\omega_{v,u} = \begin{cases} \omega_r, & n = 0 \\ 0, & n = 3h \\ \dfrac{\mp p_r}{u \mp v p_r}\omega_r, & n = 3h - 1 \\ \dfrac{\mp p_r}{u \mp v p_r}\omega_r, & n = 3h - 2 \end{cases} . \tag{4}$$

To generate stable output torque, the following equations must be satisfied (5).

$$\omega_r = \begin{cases} np_r \mp mN_s \;|=|\; vp_r \mp u \\ \dfrac{\mp np_r}{np_r \mp mN_s} = 1, \qquad n = 0 \\ \dfrac{\mp np_r}{np_r \mp mN_s}\omega_r = \dfrac{\mp p_r}{u \mp vp_r}, n = 3h-1 \\ \dfrac{\mp np_r}{np_r \mp mN_s}\omega_r = \dfrac{\mp p_r}{u \mp vp_r}, n = 3h-2 \end{cases}. \tag{5}$$

Thus, the harmonics of 5th, 19th, 29th, 43rd, 53rd, 57th, and 67th orders will primarily be utilized to generate output torque in the proposed machine. This implies that IHPMVMs can utilize these operative harmonics to transmit energy, whereas other harmonics would result in torque ripple.

If the waveform of flux linkage and back electromotive force (EMF) under no load condition are both sinusoidal, the peak values of the no-load back EMF E_m in the windings and the peak value of the armature winding current I_m can be derived as (6):

$$\begin{cases} E_m = k_1 k_w N_c \left(\sum\limits_{\substack{n=1,3,5\ldots, \\ m=0}}^{+\infty} B_{k0} + \sum\limits_{\substack{n=1, \\ m=\pm1,2,3\ldots}}^{+\infty} G_{n,m} B_{km} \right) \omega_r l D_g \\ I_m = \dfrac{\sqrt{2}\pi A_s D_g}{6N_c} \end{cases}, \tag{6}$$

where: k_l represents the no-load leakage coefficient, k_w represents the winding factor, B_{k0} and B_{km} represent the amplitude of the working harmonic magnetic flux density in the air gap, respectively. Besides, l represents the stack length, D_g represents the air gap diameter, $G_{n,m}$ is the speed ratio of other harmonics to the fundamental harmonic, and A_s represents the line loading. By neglecting the winding resistance, it can be derived from (6) that the output power of the proposed IHPMVM can be expressed as:

$$P_{\text{out}} = \frac{\sqrt{2}\pi A_s D_g^2}{4N_c} k_1 k_w N_c \left(\sum_{\substack{n=1,3,5\ldots, \\ m=0}}^{+\infty} B_{k0} + \sum_{\substack{n=1, \\ m=\pm1,2,3\ldots}}^{+\infty} G_{n,m} B_{km} \right) \omega_r l \varphi, \tag{7}$$

in which, φ is the power factor. Thus, the electromagnetic output torque can be expressed as:

$$T_{\text{out}} = \frac{\sqrt{2}\pi A_s D_g^2}{4N_c} k_1 k_w N_c \left(\sum_{\substack{n=1,3,5\ldots, \\ m=0}}^{+\infty} B_{k0} + \sum_{\substack{n=1, \\ m=\pm1,2,3\ldots}}^{+\infty} G_{n,m} B_{km} \right) l \varphi. \tag{8}$$

2.3. Magnet type evaluation

To better demonstrate the validity and feasibility of the proposed design in this paper, an evaluation of magnet types was conducted. Both conventional and proposed machines were compared under fair conditions by ensuring that they possessed the same dimensions, current

capacity, and materials, et al. Furthermore, to more significantly evaluate the reduction of RE materials in the proposed machine, both machines were designed to be at the same power level and were optimized accordingly. Table 1 lists some key parameters of the proposed machine.

Table 1. Key parameters of the proposed machine

Items	**Unit**	**Value**
Stator outer diameter	mm	170
Rotor outer diameter	mm	228
Air-gap length	mm	0.75
Phase number	–	3
Iron material	–	DW310-35
Remanence B_r of RE magnets @20°C	T	1.35
Coercivity H_c of RE magnets @20°	kA/m	1057
Remanence B_r of LRE magnets @20°	T	1.25
Coercivity H_c of LRE magnets @20°	kA/m	434
Stack length	mm	50
Stator slots	–	24
Rotor pole pairs	–	19
Current capacity	A	40
Current density	A/mm^2	7.5

The evaluation results are shown in Table 2. It can be observed that the volume of RE magnets is reduced in the proposed design, and more LRE magnets are adopted. Thus, the usage of rare earth permanent magnets has been reduced by 89.6%. Although the proposed machine utilizes a greater quantity of magnets, the overall cost has been reduced by 26% due to the lower price of LRE magnets.

Table 2. Magnet type evaluation

Items	**Unit**	**Conventional**	**Proposed**
Peak torque	per unit	1	1.01
Volume of RE magnets	cm^3	89.9	20.9
Volume of LRE magnets	cm^3	0	104
Total volume of magnets	cm^3	89.9	124.9
Magnet cost	per unit	1	0.74

3. Multi-objective optimization

The electromagnetic characteristics of the proposed machine are significantly influenced by the structural parameters of both the stator and rotor. Particularly, a multi-objective optimization is required to obtain the optimal design, meeting the design requirement. Figure 3 illustrates the parametric model of the proposed IHPMVM.

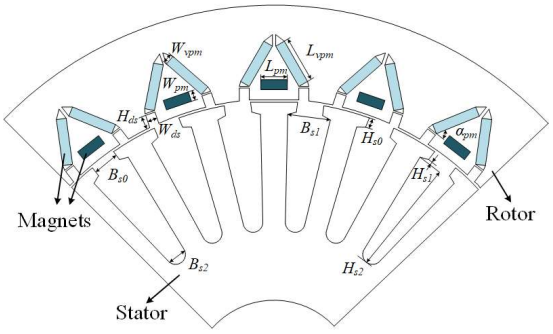

Fig. 3. Parametric model of the proposed machine

3.1. Optimization process

As shown in Fig. 4, the flow chart of the optimization process is mainly divided into the following three steps:

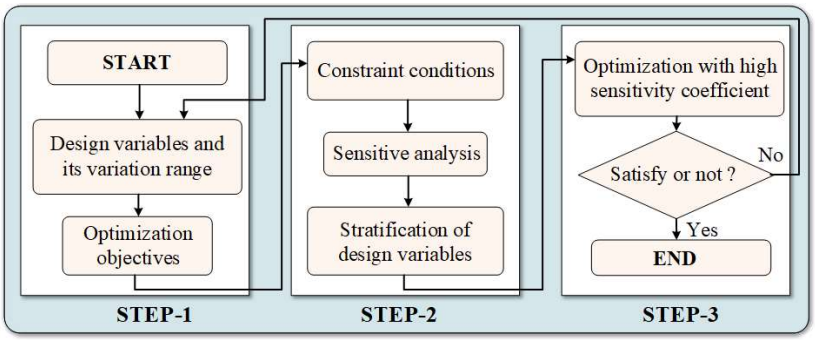

Fig. 4. Flowchart of optimization progress

1. STEP-1: Determine optimization objectives
   Based on the operational principle of the proposed IHPMVM, torque capability is crucial for PMVMs. Therefore, average torque T_{out} is selected as one of the optimization objectives. Besides, it is necessary not only to deliver a substantial average torque but also to achieve high smoothness in torque output. Therefore, the torque ripple T_{rip} may lead to significant vibration noise and is thus considered as one of the optimization objectives. Furthermore,

cogging torque is an inherent issue in PMVMs. Excessive cogging torque T_{cog} is detrimental to the stable operation of the machine, and reducing cogging torque is advantageous for lowering the noise and vibration. Hence, cogging torque should be considered as one of the optimization objectives.

2. STEP-2: Sensitive analysis
   The proposed IHPMVM is a nonlinear system with multi-physics field coupling, and the influences of parameters on electromagnetic performance are not consistent. Thus, numerous design variables will pose a challenge to the efficiency and accuracy of optimization progress. It is worth mentioning that the impact of each design variable on the optimization objective varies, some design variables have a great influence on optimization objectives, while others have little effect on them. Therefore, it is necessary to introduce more important design variables for optimization to improve the efficiency and accuracy of the optimization progress.
3. STEP-3: Multi-objective optimization
   After sensitivity analysis, a comprehensive sensitivity index is introduced to determine whether design variables have a significant impact on the optimization objectives. Thus, some sensitive design variables are selected for multi-objective optimization progress. In this paper, the multi-objective genetic algorithm (MOGA) is adopted, which is suitable for applications in multi-objective optimization of PMMs.

3.2. Sensitive analysis

Traditional optimization processes often suffer from decreased precision and longer computational times due to many design variables. Thus, a sensitivity index is introduced to characterize the degree of influence of design variables on the optimization objectives, with the following expression:

$$S(x_i) = \frac{V(E(y/x_i))}{V(y)}. \tag{9}$$

In which $E(y/x_i)$ is the average value of the optimization objective y when x_i is constant. $V(E(y/x_i))$ is the variance of $E(y/x_i)$ when $V(y)$ is the variance of y. The results are shown in Fig. 5, where a positive sensitivity index indicates a positive correlation with the optimization objectives. For the positive sensitivity index, an increase in the design variable values will lead to an increase in the optimization objective. Conversely, for a negative sensitivity index, the optimization objective will decrease with an increase in the design variable values.

To accurately characterize the comprehensive influence of individual design variables on the optimization objectives, the comprehensive sensitivity index is introduced, which can be expressed as:

$$S_{all}(x_i) = \gamma_t|S_t(x_i)| + \gamma_{cog}|S_{cog}(x_i)| + \gamma_{rp}|S_{rp}(x_i)|, \tag{10}$$

where $|S_t(x_i)|$, $|S_{cog}(x_i)|$ and $|S_{rp}(x_i)|$ are the absolute values of $S(x_i)$ to average torque, cogging torque, and torque ripple, respectively. Besides, γ_t, γ_{cog} and γ_{rp} are the weight coefficients of average torque, cogging torque, and torque ripple. In this paper, the proposed IHPMVM is designed for high torque capability. Therefore, γ_t, γ_{cog}, and γ_{rp} are set as 0.4, 0.2, and 0.2, respectively. The comprehensive sensitivity results are shown in Table 3, and design variables with the comprehensive sensitivity index quals or above 0.1 are defined as strong-sensitive design variables.

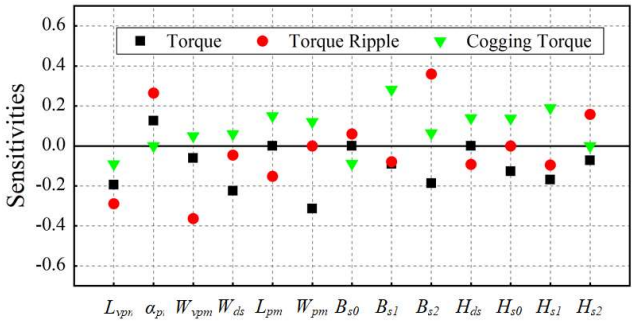

Fig. 5. Sensitive analysis

Table 3. Sensitive analysis

Design variables	**Optimization objectives**			**Comprehensive sensitivity index**	**Index > 0.1?**
	$S_t(x_i)$	$S_{rp}(x_i)$	$S_{cog}(x_i)$		
Length of LRE PMs L_{vpm}	–0.194	–0.289	-0.091	**0.154**	✓
Opening angle of LRE PMs α_{pm}	0.125	0.265	0.000	**0.103**	✓
Width of LRE PMs W_{vpm}	–0.061	–0.363	0.050	**0.107**	✓
Width of dummy slots W_{ds}	–0.225	–0.046	0.060	**0.111**	✓
Length of RE PMs L_{pm}	0.000	–0.152	0.150	0.060	
Width of RE PMs W_{pm}	–0.314	0.000	0.121	**0.150**	✓
Slot opening B_{s0}	0.000	0.060	–0.088	0.030	
Slot width (top) B_{s1}	–0.090	–0.079	0.282	**0.108**	✓
Slot width (bottom) B_{s2}	–0.187	0.360	0.064	**0.160**	✓
Height of dummy slots H_{ds}	0.000	–0.092	0.140	0.046	
Tooth tip depth-1 H_{s0}	–0.127	0.000	0.138	0.078	
Tooth tip depth-2 H_{s1}	–0.170	–0.096	0.190	**0.125**	✓
Slot depth H_{s2}	–0.072	0.157	0.000	0.060	

Based on the comprehensive sensitivity index in Table 3, strong-sensitive design variables ultimately are selected for optimization, while design variables with a low comprehensive sensitivity index will maintain initial values.

3.3. Multi-objective optimization

In this paper, the MOGA algorithm is adopted to obtain optimal objectives. To meet the design requirements, the optimization constraints is defined as:

$$\begin{cases} T_{\text{out}} \geq 80.0 \text{ N} \cdot \text{m} \\ T_{\text{rip}} \leq 5\% \\ \text{minimize } (T_{\text{cog}}) \end{cases}. \tag{11}$$

Figure 6 presents the final optimization results. Blue points in the graph denote feasible designs, while red points indicate the optimal design.

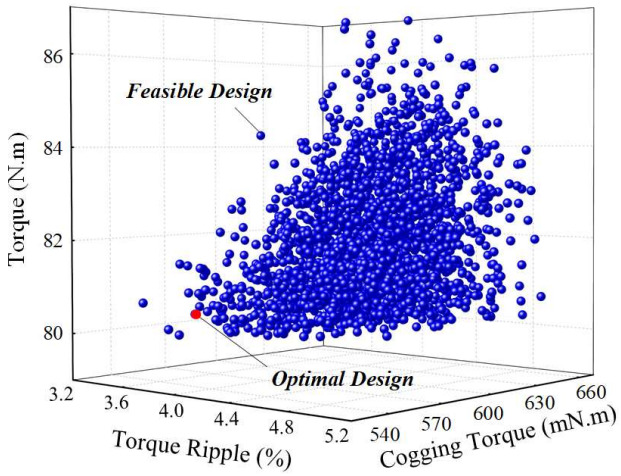

Fig. 6. Optimization results

The variation ranges of design variables and the optimization results are presented in Table 4. It can be observed that the optimized average torque, cogging torque, and torque ripple are 80.4 N·m, 370 mN·m, and 3.2%.

Table 4. Design variables and variation range

Design variables	**Ranges**	**Unit**	**Initial**	**Optimal**
L_{vpm}	[12, 15]	mm	14.0	14.8
α_{pm}	[58, 62]	deg	60.0	59.5
W_{vpm}	[2.3, 3.8]	mm	3.0	3.7
W_{ds}	[2.5, 3.5]	mm	3	2.8
W_{pm}	[2.3, 3.8]	mm	8.0	2.7
B_{s1}	[7, 13]	mm	13.0	12.4
B_{s2}	[6, 10]	mm	6.0	6.1
H_{s1}	[1.5, 3]	mm	2.0	1.9
Torque	–	N·m	65.8	80.4
Cogging torque	–	mN·m	760	370
Torque ripple	–	%	8.4	3.2

4. Preliminary electromagnetic performance

To validate the effectiveness and feasibility of the multi-objective optimization, preliminary electromagnetic performances of the proposed machine before and after optimization are analyzed and compared using the finite element (FE) method. The initial and optimal design have the same dimensions, current capacity, and materials, etc. The FE results presented in this paper were obtained using ANSYS Electronics Suite 2024 R1.

4.1. Open-circuit characteristics

Figure 7 shows magnetic flux density distributions of the initial and optimal designs of the proposed machine under open-circuit conditions. The magnetic flux densities of the stator teeth and stator yoke are within an acceptable range. However, due to the special slot/pole combination, asymmetrical distributions of magnetic field distribution are presented.

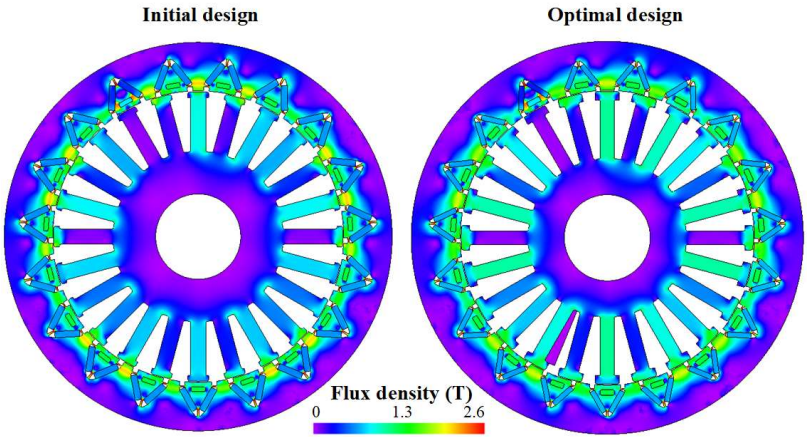

Fig. 7. Open-circuit flux density distributions

Figure 8 represents the flux lines distribution under open-circuit conditions of the proposed machine. It can be seen that the flux lines flow into the stator side through the PMs, avoiding the dummy slots. Thus, effective fluxes enter the stator side. It is also proved that dummy slots can reduce the self-leakage flux of magnets.

Figure 9(a) shows the open-circuit back EMF waveforms at 300 rpm for both the initial and optimal designs. It can be observed that both back EMF waveforms exhibit good sinusoidal properties. Besides, the amplitude of the open-circuit back EMF of the optimal design is decreased from 38.4 V to 34.5 V after optimization.

The harmonic analyses of the back EMF waveforms of the initial and optimal designs are presented in Fig. 9(b). The total harmonic distortion (THD) of the open-circuit back EMF waveforms before and after optimization are 2.48% and 3.21%, respectively. The distortion is primarily caused by the 3rd and 5th harmonics, with their amplitudes significantly smaller than the fundamental harmonic. Thus, it can be observed that the 3rd harmonic exerts the greatest influence on the distortions of the open-circuit back EMF among all harmonics.

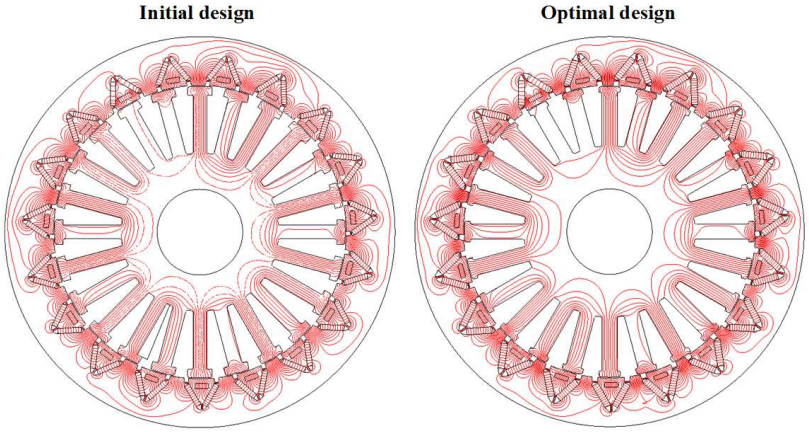

Fig. 8. Flux lines distributions

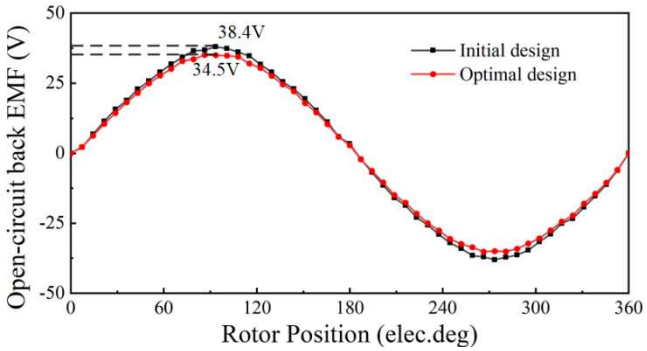

(a)

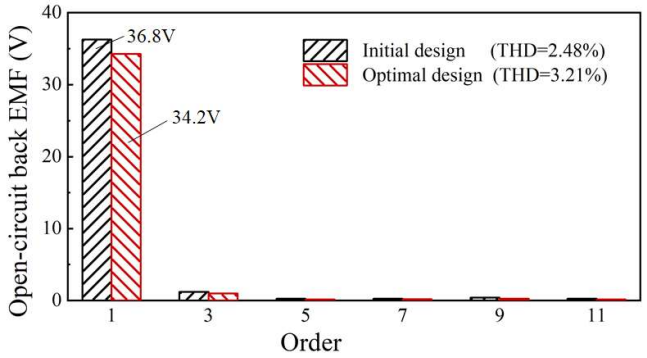

(b)

Fig. 9. Open-circuit back EMF: (a) initial design; (b) optimal design

4.2. On-load air-gap flux density

Figure 10 shows the air-gap flux density waveforms of both the initial and optimal designs of the proposed IHPMVM. The air-gap flux density waveform of the IHPMVM differs from that of conventional PMs, owing to the flux modulation effect. Besides, the air-gap flux density waveform is more complex due to the significant harmonic components. It can be observed from Fig. 10 that the amplitude of the air-gap flux density of the optimal design is increased relative to the initial design, thus validating the effectiveness of the optimization.

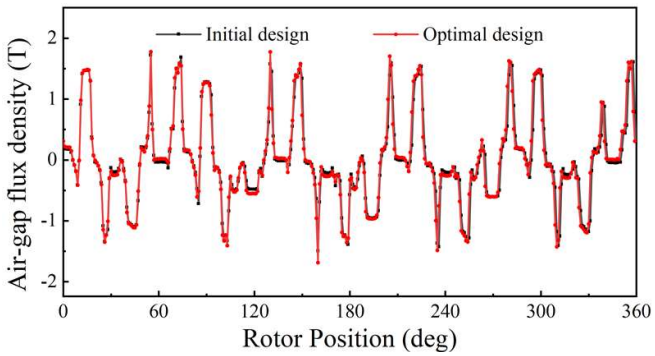

Fig. 10. On-load air-gap flux density

Furthermore, as shown in Fig. 11, the harmonic analysis of the air-gap flux density for the proposed IHPMVM reveals the working harmonic components are the 5th, 19th, 29th, 43rd, 53rd, and 67th harmonics.

Particularly, the 19th harmonic component, directly generated by the magnets, exhibits the highest amplitude. Besides, the amplitude of the 5th harmonic in the initial design is 0.61 T, while in the optimal design, it reaches 0.68 T.

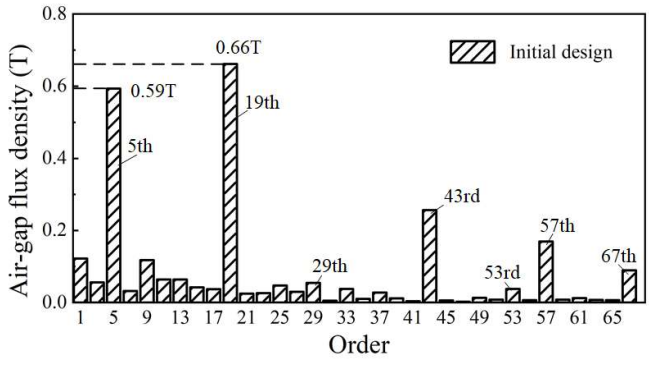

(a)

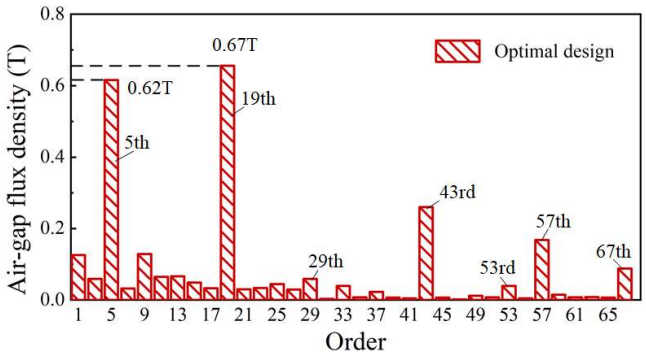

(b)

Fig. 11. Harmonic analysis of air-gap flux densities: (a) initial design; (b) optimal design

4.3. Torque capabilities

Figure 12 shows the cogging torque waveforms of the initial design and optimal design of the proposed machine. It can be observed that the peak-to-peak value of cogging torque for the initial design is approximately 760 mN·m, while the peak-to-peak value for the optimal design is 370 mN·m. It is evident that the cogging torque significantly decreases after optimization.

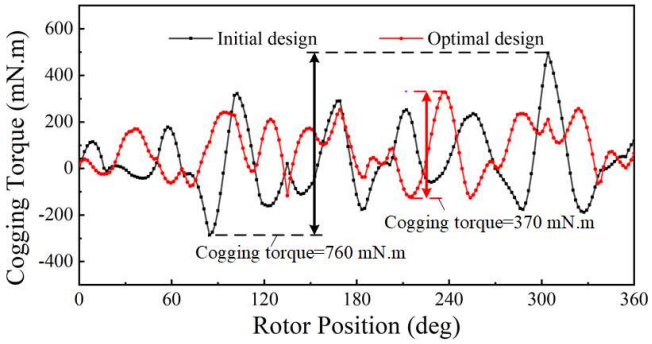

Fig. 12. Waveforms of cogging torque

The transient torque waveforms of the proposed machine under peak conditions are depicted in Fig. 13, with a three-phase sinusoidal current applied to the winding, disregarding the effects of harmonics and other factors.

It can be found that the average output torque of the initial design is 65.8 N·m, with a torque ripple of 8.4%. Besides, the average output torque of the optimal design is 80.4 N·m, with a torque ripple of 3.2%. The average torque of the optimal design has increased by 22.2% compared to the initial design, and its torque ripple has been reduced by 5.2%, confirming the effectiveness of the optimization process. In addition, as the armature current increases, the average torque of the initial and optimal designs also increases, as shown in Fig. 14. It is worth noting that the trend of the average torque increase with current is less pronounced in the initial design due to magnetic saturation, whereas the optimal design suffers less serious magnetic saturation.

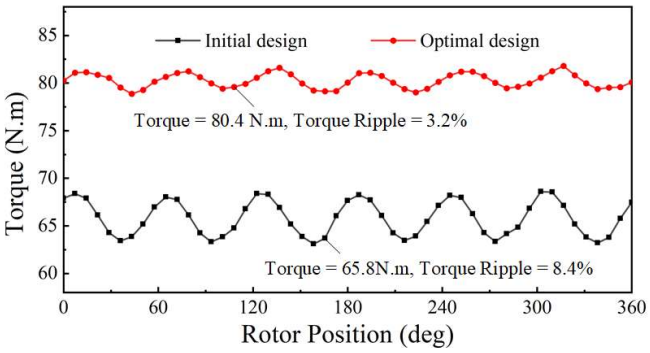

Fig. 13. Waveforms of output torque

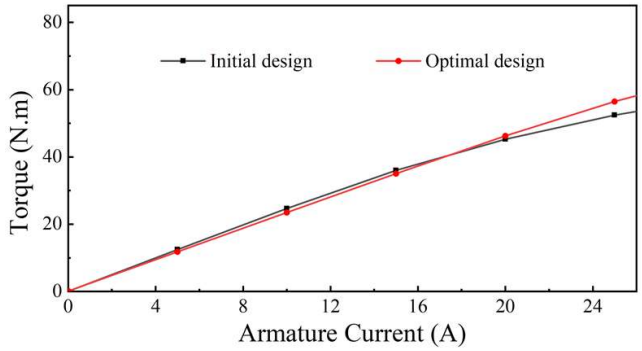

Fig. 14. Average torques versus armature currents

The average torques under different current angles are shown in Fig. 15.

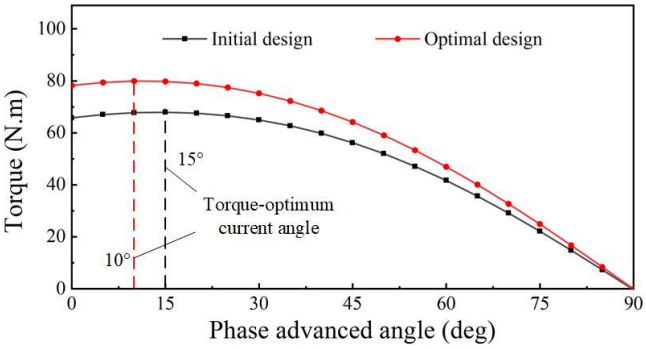

Fig. 15. Torque-optimum current angle

It can be observed that the torque-optimum current angles of the initial and optimal designs are 15° and 10°, respectively. Therefore, it can be inferred that the larger reluctance torque component in the initial design is attributable to its interior PM structure.

4.4. Demagnetization evaluation

In the proposed design, LRE magnets with low coercivity force are adopted. Therefore, it is necessary to evaluate the demagnetization withstand capability of the IHPMVM. In this paper, the evaluation is conducted under deep flux weakening conditions.

Figure 16 depicts the demagnetization cloud map distribution of the magnets under flux weakening conditions.

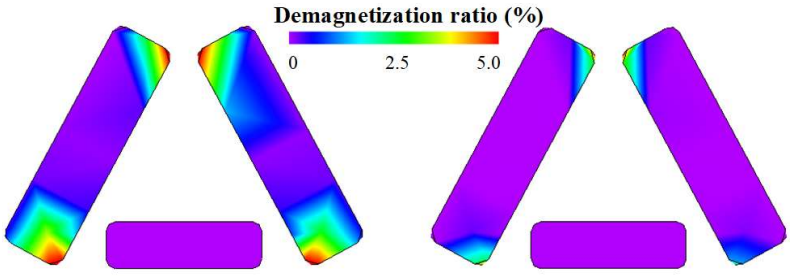

(a) (b)

Fig. 16. Demagnetization ratio: (a) initial design; (b) optimal design

The initial design exhibits severe demagnetization at the edges of the LRE magnets, whereas there is almost no demagnetization observed in the RE magnets. Conversely, the optimal design shows negligible demagnetization at the edges of the LRE magnets, meeting the design requirements. This is attributed to the RE magnets effectively preventing demagnetization of the LRE magnets.

4.5. Efficiency characteristic

The efficiency characteristics of the proposed machine before and after optimization are shown in Fig. 17. It can be observed that the peak efficiency of the optimized IHPMVM is 94.3%, compared to 92.9% before optimization, representing an improvement of 1.4%. Furthermore, the proportion of the high-efficiency region for the proposed machine before optimization is 53.4%, while the proportion after optimization is 46.3%, indicating an increase of 7.1%. Thus, the effectiveness of the optimization progress has been validated.

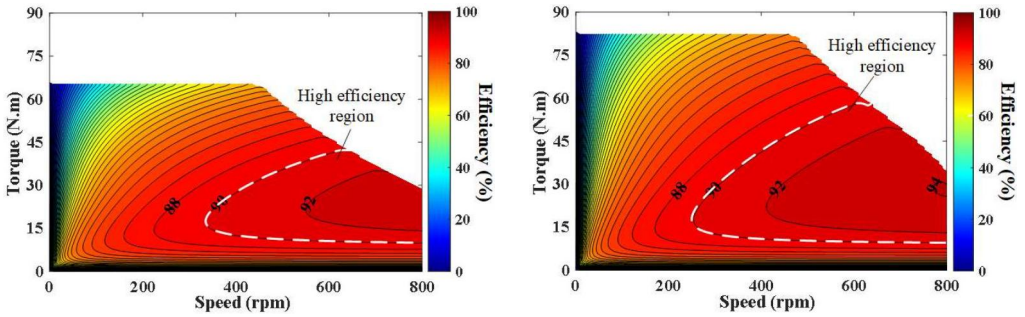

(a) (b)

Fig. 17. Efficiency maps: (a) initial design; (b) optimal design

5. Conclusions

In this paper, a novel improved hybrid PM Vernier machine (IHPMVM) is proposed, in which the consumptions of RE materials can be reduced by using the LRE magnets. Notably, the improved design also has a good magnetic flux concentrated effect, resulting in high torque-density characteristics. The following conclusions can be drawn:

1. The proposed IHPMVM can reduce the usage of RE materials while achieving high torque density characteristics with LRE materials.
2. The proposed hybrid magnet arrangement has a good demagnetization withstand capability, with RE magnets shielding LRE magnets from demagnetization.
3. It is evident from the comparison of electromagnetic performance before and after optimization that the optimal design has significantly improved the output torque, cogging torque, and torque ripple, confirming the effectiveness of the optimization.

References

[1] Zhu Z.Q., Howe D., *Electrical machines and drives for electric, hybrid, and fuel cell vehicles*, Proceedings of the IEEE, vol. 95, no. 4, pp. 746–765 (2007), DOI: 10.1109/JPROC.2006.892482.

[2] Chau K.T., Chan C.C., Liu C., *Overview of permanent-magnet brushless drives for electric and hybrid electric vehicles*, IEEE Transactions on Industrial Electronics, vol. 55, no. 6, pp. 2246–2257 (2008), DOI: 10.1109/TIE.2008.918403.

[3] Wang H., Xue Y., Du J., Li H., *Design and evaluation of modular stator hybrid-excitation* switched *reluctance motor for torque performance improvement*, IEEE Transactions on Industrial Electronics, vol. 71, no. 10, pp. 12814–12823 (2024), DOI: 10.1109/TIE.2024.3357899.

[4] Polinder H., van der Pijl F.F.A., de Vilder G -J., Tavner P.J., *Comparison of direct-drive and geared generator concepts for wind turbines*, IEEE Transactions on Energy Conversion, vol. 21, no. 3, pp. 725–733 (2006), DOI: 10.1109/TEC.2006.875476.

[5] Liu Z., Tang C., Fang Y., Pfister P.-D., *A direct-drive permanent-magnet motor selective compliance assembly robot arm: modeling, motion control, and trajectory optimization based on direct collocation method*, IEEE Access, vol. 11, pp. 123862–123875 (2023), DOI: 10.1109/ACCESS.2023.3329883.

[6] Ishizaki A., Tanaka T., Takasaki K., Nishikata S., *Theory and optimum design of PM Vernier motor*, 1995 Seventh International Conference on Electrical Machines and Drives, Durham, UK, pp. 208–212 (1995), DOI: 10.1049/cp:19950864.

[7] Kim B., Lipo T.A., *Operation and design principles of a PM Vernier motor*, IEEE Transactions on Industry Applications, vol. 50, no. 6, pp. 3656–3663 (2014), DOI: 10.1109/TIA.2014.2313693.

[8] Toba A., Lipo T.A., *Generic torque-maximizing design methodology of surface permanent-magnet Vernier machine*, IEEE Transactions on Industry Applications, vol. 36, no. 6, pp. 1539–1546 (2000), DOI: 10.1109/28.887204.

[9] Du Z.S., Lipo T.A., *Torque performance comparison between a ferrite magnet Vernier motor and an industrial interior permanent magnet machine*, IEEE Transactions on Industry Applications, vol. 53, no. 3, pp. 2088–2097 (2017), DOI: 10.1109/TIA.2017.2673812.

[10] Zhu Z.Q., Liu Y., *Analysis of air-gap field modulation and magnetic gearing effect in fractional-slot concentrated-winding permanent magnet synchronous machines*, IEEE Transactions on Industrial Electronics, vol. 65, no. 5, pp. 3688–3698 (2018), DOI: 10.1109/TIE.2017.2758747.

[11] Fan D., Quan L., Zhu X., Xiang Z., Que H., *Airgap-harmonic-based multilevel design and optimization of a double-stator flux-modulated permanent-magnet motor*, IEEE Transactions on Industrial Electronics, vol. 68, no. 11, pp. 10534–10545 (2021), DOI: 10.1109/TIE.2020.3039207.

[12] Yu Z., Kong W., Li D., Qu R., Gan C., *Power factor analysis and maximum power factor control strategy for six-phase DC-biased Vernier reluctance machines*, IEEE Transactions on Industry Applications, vol. 55, no. 5, pp. 4643–4652 (2019), DOI: 10.1109/TIA.2019.2923593.

[13] Cheng M., Wen H., Han P., Zhu X., *Analysis of air-gap field modulation principle of simple salient poles*, IEEE Transactions on Industrial Electronics, vol. 66, no. 4, pp. 2628–2638 (2019), DOI: 10.1109/TIE.2018.2842741.

[14] Zhao W., Gu C., Chen Q., Ji J., Xu D., *Remedial phase-angle control of a five-phase fault-tolerant permanent-magnet Vernier machine with short-circuit fault*, CES Transactions on Electrical Machines and Systems, vol. 1, no. 1, pp. 83–88 (2017), DOI: 10.23919/TEMS.2017.7911112.

[15] Zhao X., Niu S., Fu W.N., *Torque component quantification and design guideline for dual permanent magnet Vernier machine*, IEEE Transactions on Magnetics, vol. 55, no. 6, pp. 1–5 (2019), DOI: 10.1109/TMAG.2019.2894872.

[16] Niu S., Ho S.L., Fu W.N., *A novel stator and rotor dual PM Vernier motor with space vector pulse width modulation*, IEEE Transactions on Magnetics, vol. 50, no. 2, pp. 805–808 (2014), DOI: 10.1109/TMAG.2013.2280758.

[17] Xu L., Zhao W., Liu G., Song C., *Design optimization of a spoke-type permanent-magnet Vernier machine for torque density and power factor improvement*, IEEE Transactions on Vehicular Technology, vol. 68, no. 4, pp. 3446–3456 (2019), DOI: 10.1109/TVT.2019.2902729.

[18] Liu W., Lipo T.A., *Analysis of consequent pole spoke type Vernier permanent magnet machine with alternating flux barrier design*, IEEE Transactions on Industry Applications, vol. 54, no. 6, pp. 5918–5929 (2018), DOI: 10.1109/TIA.2018.2856579.

[19] Allahyari A., Torkaman H., *A novel high-performance consequent-pole dual rotor permanent magnet Vernier machine*, IEEE Transactions on Energy Conversion, vol. 35, no. 3, pp. 1238–1246 (2020), DOI: 10.1109/TEC.2020.2980146.

[20] Jang D., Chang J., *Investigation of doubly salient structure for permanent magnet Vernier machines using flux modulation effects*, IEEE Transactions on Energy Conversion, vol. 34, no. 4, pp. 2019–2028 (2019), DOI: 10.1109/TEC.2019.2936022.

[21] Jahns T., *Getting rare-earth magnets out of EV traction machines: A review of the many approaches being pursued to minimize or eliminate rare-earth magnets from future EV drivetrains*, IEEE Electrification Magazine, vol. 5, no. 1, pp. 6–18 (2017), DOI: 10.1109/MELE.2016.2644280.

[22] Boldea I., Tutelea L.N., Parsa L., Dorrell D., *Automotive electric propulsion systems with reduced or no permanent magnets: an overview*, IEEE Transactions on Industrial Electronics, vol. 61, no. 10, pp. 5696–5711 (2014), DOI: 10.1109/TIE.2014.2301754.

[23] Chen Q., Xu G., Zhai F., Liu G., *A novel spoke-type PM motor with auxiliary salient poles for low torque pulsation*, IEEE Transactions on Industrial Electronics, vol. 67, no. 6, pp. 4762–4773 (2020), DOI: 10.1109/TIE.2019.2924864.

[24] Fontana M., Bianchi N., *Design and analysis of normal saliency IPM spoke motor*, IEEE Transactions on Industry Applications, vol. 56, no. 4, pp. 3625–3635 (2020), DOI: 10.1109/TIA.2020.2988842.

[25] Seok C., Choi H., Seo J., *Design and analysis of a novel spoke-type motor to reduce the use of rare-earth magnet materials*, IET Electric Power Application, vol. 15, no. 11, pp. 1479–1487 (2021), DOI: 10.1049/elp2.12109.

[26] Zhao W., Yang Z., Liu Y., Wang X., *Analysis of a novel surface-mounted permanent magnet motor with hybrid magnets for low cost and low torque pulsation*, IEEE Transactions on Magnetics, vol. 57, no. 6, pp. 1–4 (2021), DOI: 10.1109/TMAG.2021.3057391.

[27] Zhu X., *Torque component redistribution and enhancement for hybrid permanent magnet motor with permanent magnet offset placement*, IEEE Transactions on Transportation Electrification, vol. 9, no. 1, pp. 631–641 (2023), DOI: 10.1109/TTE.2022.3177745.